THESIS FOR THE DEGREE OF LICENTIATE OF ENGINEERING

in

Thermo and Fluid Dynamics

Large-Eddy Simulation of the Flow around Simplified High-Speed Trains under Side Wind Conditions

HASSAN NASR HEMIDA

Department of Applied Mechanics

CHALMERS UNIVERSITY OF TECHNOLOGY

Göteborg, Sweden, 2006

Large-Eddy Simulation of the Flow around Simplified High-Speed Trains under Side Wind Conditions

HASSAN NASR HEMIDA

THESIS FOR LICENTIATE OF ENGINEERING no 2006:06
ISSN 1652-8565

Department of Applied Mechanics
Chalmers University of Technology
SE-412 96 Göteborg, Sweden
Phone +46-(0)31-7721400
Fax: +46-(0)31-180976

Printed at Chalmers Reproservice
Göteborg, Sweden 2006

Large-Eddy Simulation of the Flow around Simplified High-Speed Trains under Side Wind Conditions

by

Hassan Nasr Hemida

hemida@chalmers.se

Division of Fluid Dynamics

Department of Applied Mechanics

Chalmers University of Technology

SE-412 96 Göteborg

Sweden

Abstract

The new generation of high-speed trains, which are characterized by light weight, are at high risk of overturning or derailment when cruising in a strong side wind. With the introduction of high-speed trains traveling at 250 km/hr and more, the likelihood of such an accident has increased. However, prevention of the unwanted influences of a side wind requires that the flow structures on the train surface and around it are fully understood in both the instantaneous and the time-averaged flow.

In this work, large-eddy simulation (LES) using the standard Smagorinsky sub-grid scale (SGS) model with model constant $C_s = 0.1$ is used to compute the side-wind flow around stationary generic train models. The side-wind flow is obtained at three different yaw angles, 30^o, 35^o and 90^o. LES gives results that agree well with the experimental observations and displays many flow features that were not observed in the experiments. The flow around high-speed trains involves many small structures due to the instabilities of the shear layers that contribute to the time varying values of the forces around the train. In the results of LES, we have studied the time-dependent behavior of these structures and their impact on the train surface pressure and thus on the aerodynamic coefficients. The influence of the train nose shape on the flow field under side-wind conditions is investigated. Our LES results show that the train nose shape determines to a large extent the characteristics of the wake structures and their associated frequencies. The investigations conducted in the present work focus on the wake structures and their influence on the aerodynamic coefficients.

Acknowledgments

This work would not have been possible without the support of a number of organizations and individuals. The research was carried out at the Division of Fluid Dynamics, Department of Applied Mechanics, Chalmers University of Technology. This work was supported by the Swedish Agency for Innovation System (VINNOVA), Bombardier Transportation, and Scania. Computer time on HPC2N (High Performance Computing Center North), NSC (National Supercomputer Center in Sweden), HIVE supercomputer at SWEGRID, and HELIOS supercomputer provided by UNICC at Chalmers is gratefully acknowledged.

I would like to express my sincere gratitude to my supervisor, Dr. Siniša Krajnović, for sharing some of his profound knowledge in computational fluid dynamics with me. This thesis would never have reached this point without his enlightening discussions and brilliant advice.

I express my sincere appreciation to my examiner, Professor Lars Davidson, who believed in me and introduced me to the research field and gave me the opportunity to undertake the PhD program in his group. Thanks Lars for all good advice and encouragement.

I would like to thank Dr. Håkan Nilson for his time and wonderful help and assistance in solving some CFD code-related problems.

My thanks to all of my colleagues, especially Darioush Gouhari, Kristian Wallblad and Walter Gyllenram for the helpful discussions and fixing my computer-related problems.

The interesting and simulating discussions that arose at the steering group meetings are gratefully acknowledged, and my thanks go to Per Johnson and Stephen Conway from Scania and Ben Diedrichs from Bombardier Transportation.

My former examiner, Professor Essam Hamdi, head of the Electrical Machines and Derive Systems group, was the first to grant me the chance to be a student at Chalmers. Thank you Essam for your understanding and for the help and the support you always offer.

My warmest and deepest sense of gratitude goes to my family, Fainan, Mayar and Momen, for their love and support.

Nomenclature

Upper-case Roman

A_{ij}	second order tensor
C_d	drag force coefficient
C_l	lift force coefficient
C_s	side force coefficient and Smagorinsky model coefficient
C_p	local pressure coefficient
D	train height
F_d	drag force
F_l	lift force
F_s	side force
J_{ij}	Jacobian tensor
L	train length
M_p	pitching moment
M_r	rolling moment
M_y	yawing moment
P	first invariant of the velocity gradient
Q	second invariant of the velocity gradient
R	third invariant of the velocity gradient
Re	Reynolds number
S_{ij}	strain rate tensor
St	Strouhal number
U	velocity

Lower-case Roman

$a_i,\ b_i$	vectors in space
c_i	constant in Eq.3.16
f	frequency
p	pressure
t	time
t^*	dimensionless time unit
u_i	Cartesian components of velocity vector

$x,\ y,\ z$	Cartesian coordinate vector components

Upper-case Greek

Δ	filter width and matrix discriminant
Δt	time step
Ω_{ij}	rotation tensor

Lower-case Greek

δ_{ij}	Kronecker delta
θ	angle from in a train cross-section
λ	tensor eigenvalues
μ	viscosity
ν	kinematic viscosity ($\nu = \mu/\rho$)
ν_t	turbulent kinematic viscosity
ρ	density
σ_{ij}	viscous stress tensor
τ_{ij}	subgrid scale stress tensor

Subscripts

t	turbulent quantity
o	initial condition
∞	free stream or ambient conditions

Superscripts

SGS	subgrid scale
$-$	spatially filtered quantity

Abbreviations

CFD	Computational Fluid Dynamics
CFL	Courant-Friedrichs-Levy
LES	Large Eddy Simulation
MPI	Message Passing Interface
RANS	Reynolds Averaged Navier-Stokes

Contents

Chapter 1

Introduction

1.1 Motivation

When a high-speed train cruises in a side wind, the effective side wind is strong even if the magnitude of the side-wind velocity is low. The effective side wind is the result of the train speed and the side-wind speed. The angle between the effective side-wind direction and the train cruising direction is the yaw angle, as shown in Fig. 1.1. The value of this angle is determined by the train cruising speed, the side-wind speed and the side-wind direction. Normally, side wind yaw angles are below 40^o owing to relatively low-speed side winds compared to the train speed. However, it is possible to find high-speed trains that are cruise at larger yaw angles, e.g. when they exit from tunnels or when a strong side wind has a strong component in the direction of the train motion.

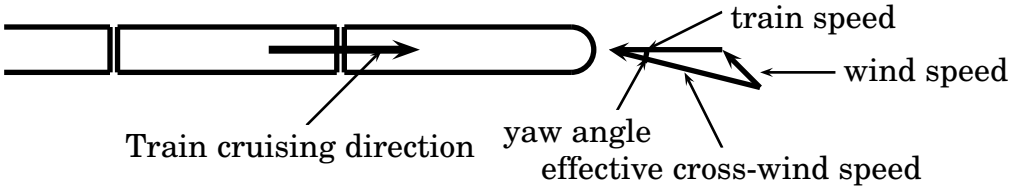

Figure 1.1: Effective side wind

The new generation of high-speed trains is light in weight in order to provide high acceleration and to reduce the energy necessary to overcome gravity and friction forces. When these trains cruise in a strong side wind, there is a stagnation region with high pressure on the streamwise face while a region of low pressure is formed on the lee

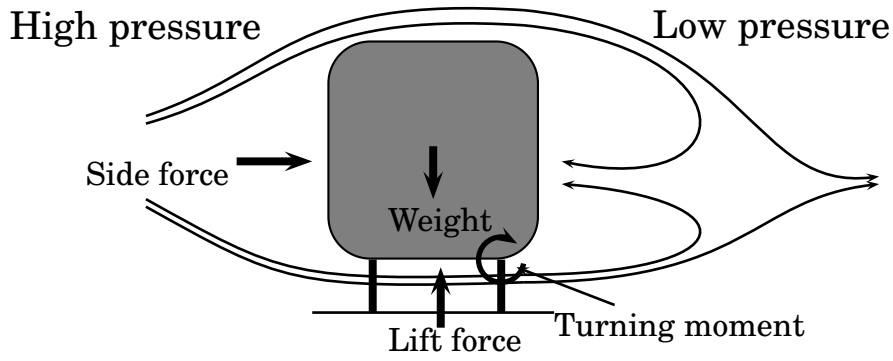

Figure 1.2: Aerodynamic forces and moments due to side wind

side due to the recirculation regions in the wake flow. In addition, the flow moves over the train roof at high velocity, making a region of low pressure on the upper side of the train. Due to these pressure differences, the high-speed trains experience strong aerodynamic forces and moments such as side and lift forces and a yaw moment, as shown in Fig. 1.2. In such conditions, the high-speed trains are at high risk of overturning or derailment.

It is well known that the shape of the vehicle determines the influence of the side winds on the vehicle stability. Thus the vehicle's side wind resistance can be improved by adjusting its design. Previous experimental studies have concentrated mainly on the vehicle's response to the side wind and not much on understanding the flow mechanisms. Prevention of the unwanted influences of a side wind requires that flow structures on the train surface and around it are fully understood in both the instantaneous and the time-averaged flow. Unsteady flow past a train in a side wind has been the object of numerous experimental investigations [1, 2, 3, 4, 5, 6, 7]. The primary interest in these investigations was the measurement of some integral parameters such as drag, lift and side force coefficients together with measurements of the natural wind characteristics around the train. Some other researchers have investigated the flow structures numerically [8, 9] to obtain a better understanding of the flow behavior. Most of these studies are based on Reynolds-averaged Naiver-Stokes (RANS) equations or time varying RANS (URANS). Since the side-wind instability is a consequence of the unsteadiness of the flow field around the train, an accurate time-dependent solution is necessary. Diedrichs [10] made a comprehensive

literature review of computational methods for cross-wind stability of railway trains. His study showed that most of the previous side-wind investigations are based on the time-averaged solution. Here only the mean flow is explored and the instantaneous information is lost.

1.2 Aerodynamic coefficients

As mentioned before, when high-speed trains cruise in a side wind they experience aerodynamic forces and moments. The aerodynamic forces are the drag force, F_d, which resists the forward motion of the train, lift force, F_l, which acts upward and tends to raise the train of the rail, and the side force, F_s, which pushes the train from the side. The latter is a result of the side wind. The aerodynamic moments that arise due to side wind are the rolling moment, M_r, the pithing moment, M_p, and the yawing moment, M_y. Figure 1.3 shows the different aerodynamic forces and moments on a train subjected to a side wind. The magnitude of these forces and moments depends on the Reynolds number and the shape of the train.

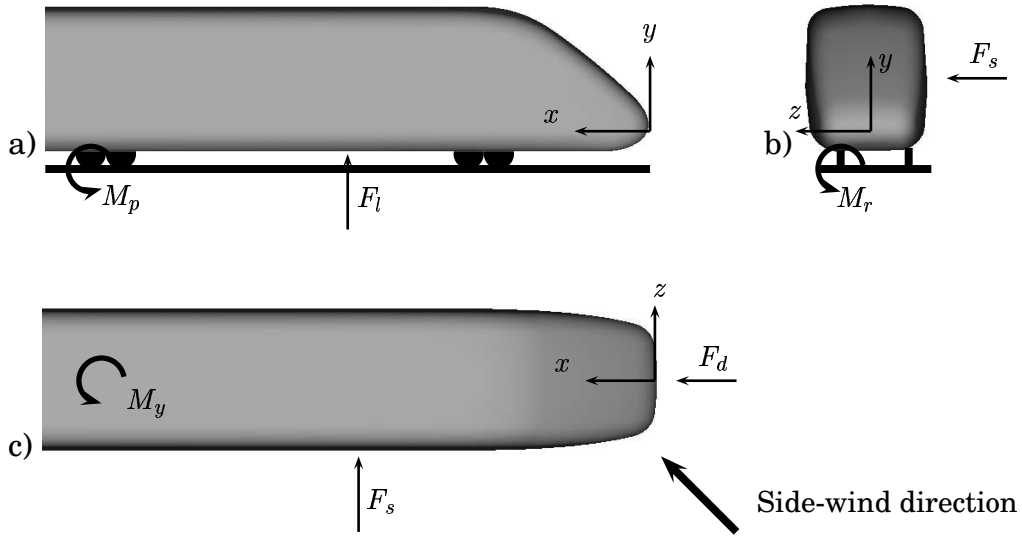

Figure 1.3: Forces and moments acting on trains under the influence of a side wind.

It is useful to have a simple means to compare the aerodynamic forces produced by different train shapes regardless of their size or driving speed. This is conveniently provided by factors called aerodynamic coefficients, which mainly depend on the shape of the train and

side wind direction. The drag coefficient, C_d, the lift coefficient, C_l, and the side force coefficient, C_s, are defined as:

$$C_d = \frac{\int p_s dA_x}{\frac{1}{2}\rho {U_\infty}^2 A_x}, \tag{1.1}$$

$$C_l = \frac{\int p_s dA_y}{\frac{1}{2}\rho {U_\infty}^2 A_y} \tag{1.2}$$

and

$$C_s = \frac{\int p_s dA_z}{\frac{1}{2}\rho {U_\infty}^2 A_z} \tag{1.3}$$

where p_s is the surface pressure, and A_x, A_y and A_z are the projected surface areas in the x, y and z directions, respectively.

In certain flow regimes, the effect of Reynolds number on the aerodynamic coefficients can be quite pronounced. The coefficients can change dramatically over the Reynolds number region, which encompasses transition from laminar to turbulent boundary layers. However, in other flow regimes, the effect of the Reynolds number is much weaker. As a result, aerodynamic coefficients are often considered to be rather weak functions of Reynolds number and a strong function of yaw angle.

It is convenient to express the pressure distribution in terms of the pressure coefficient, C_p, which is defined as:

$$C_p = \frac{p - p_\infty}{\frac{1}{2}\rho {U_\infty}^2} \tag{1.4}$$

where p is the local static pressure, U_∞ is the free-stream velocity and p_∞ is the free-stream static pressure. The difference between the local static pressure, p, and the free-stream static pressure, p_∞, depends directly on the dynamic pressure of the free stream, $1/2\rho {U_\infty}^2$. Therefore, the pressure coefficient remains constant at all speeds.

1.3 Flow Structures Around Trains

Copley [5] investigated the influence of Reynolds number on the flow field around a train when it is subjected to a cross wind. He found that, for very low Reynolds number, the flow around the train is laminar everywhere and remains attached to the train surface. Increasing

the Reynolds number results in a separation on the roof-side streamwise edge and the detachment of the flow from the face, as shown in Fig. 1.4.a. At the same time, the wake begins to shed vortices in a regular fashion. A further increase in Reynolds number makes the flow fully turbulent in the wake and in the separation region over the roof-side face. At some critical Reynolds number, the flow reattaches to the face, forming a separation bubble, as shown in Fig. 1.4.b. For higher Reynolds number, this separation bubble is suppressed and the flow over the roof-side face is fully attached, as shown in Fig. 1.4.c. However, although the influence of a train nose shape is believed to play an important role in the flow structures and aerodynamics of high-speed trains and influences the value of the Reynolds number at which the flow becomes fully attached, it has not been properly investigated in previous studies.

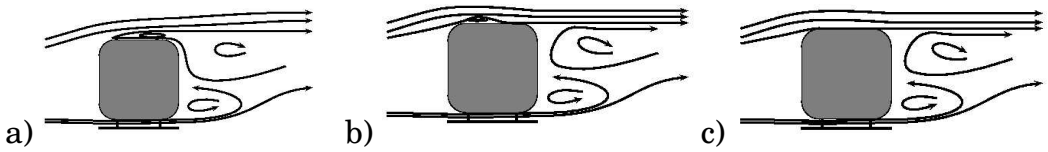

Figure 1.4: Reynolds number effect on the flow structures around train under cross-wind conditions.

Numerical and experimental studies of the flow around bluff bodies [11, 12, 13, 14, 15] show that such flows are highly unsteady and three-dimensional. Moreover, when the Reynolds number is high enough to obtain a fully turbulent flow in the shear layers and in the wake, two main instability modes are present in the wake. The first is the large-scale shedding in the wake, and it manifests itself as a progressive wave motion with alternate fluctuations produced by the shear present at the limit between the recirculation zone and the exterior fluid. These fluctuations determine the periodic shedding of the vortices that form behind the bluff body. The second high frequency mode is so called spiral mode, which is associated with the small-scale shear-layer Kelvin-Helmholtz instability on the periphery of the recirculation region where shear flow is present, as shown in Fig. 1.5. This instability is responsible for the distortion of the large vortex structures, shedding of the vortex tubes in a quasi-coherent fashion inside the detached shear layers, production of the small scales, and, eventually, transition to turbulence in the wake (for more detail see [15]).

Capturing these structures and the investigating the flow features

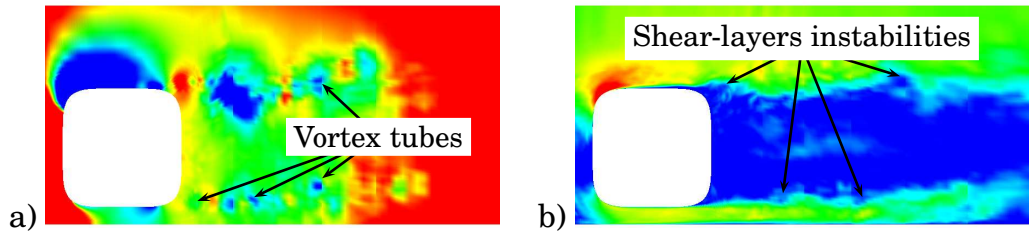

Figure 1.5: Cross-section of the LES flow around trains in a cross-wind showing the shear-layer instabilities colored by (a) the instantaneous static pressure and (b) the magnitude of the instantaneous velocity vector.

require simulation methods that resolve, rather than model, the main dynamics governing the flow. Numerical solutions using URANS are not able to catch these high frequency modes since the Reynolds stresses representing the turbulence in URANS are modeled with a turbulence model. Finding a true representation of the flow is dependent on the turbulence model used. Moreover, it is difficult to define a model that can accurately represent the Reynolds stresses in the region of separated flow, such as the wake behind a train. The discretization schemes play important roles in determining these structures. Since the high frequency modes in the train boundary layers and shear layers are important in side-wind simulations, the convective flux, the viscous diffusion and the sub-grid fluxes should be approximated by a second-order-accurate central difference scheme to reduce the numerical dissipation that arises from using upwind schemes. This dissipation suppresses the formation of the small eddies and hence the formation of high frequency modes.

Chapter 2

Governing Equations and Numerical Method

Since side-wind stability is a consequence of flow unsteadiness, an understanding of the instantaneous flow is crucial to understanding of flow around high-speed trains. Thus a time-dependent method, such as LES, should be used in order to provide instantaneous information about the flow. LES has already been proven to be a reliable technique in the prediction of flows around simplified road vehicles [16, 17]. Until recently, it was impossible to numerically predict the time-dependent flow around a train model even at moderate Reynolds numbers. In recent years, the increase in computer capability has made these simulations possible with LES.

It is worth mentioning that complicated flow structures develop in the wake region behind trains. These wake structures are dominated by large turbulent structures. Most of these structures are resolved using LES, and only the influence of the scales smaller than the computational cells is modeled. Although LES is computationally more expensive than RANS, it can provide more accurate time-averaged results and also give information on the instantaneous flow that is out of the reach of RANS. This chapter presents the governing LES equation and the subgrid-scale model used in the simulation. This is followed by a presentation of the numerical scheme used and the boundary conditions.

2.1 Governing Equations

In LES, the large eddies are computed directly and the influences of the small-scale eddies on the large-scale eddies are modeled. The incompressible Navier-Stokes equations and the continuity equation are

filtered using an implicit spatial filter. The resulting filtered equations are:

$$\frac{\partial \bar{u}_i}{\partial t} + \frac{\partial}{\partial x_j}(\bar{u}_i \bar{u}_j) = -\frac{1}{\rho}\frac{\partial \bar{p}}{\partial x_i} + \nu \frac{\partial^2 \bar{u}_i}{\partial x_j x_j} - \frac{\partial \tau_{ij}}{\partial x_j} \tag{2.1}$$

and

$$\frac{\partial \bar{u}_i}{\partial x_i} = 0. \tag{2.2}$$

Here, $\bar{u}_i$ and $\bar{p}$ are the resolved filtered velocity and pressure, respectively, while $\tau_{ij} = \overline{u_i u_j} - \bar{u}_i \bar{u}_j$ are the sub-grid scale (SGS) stresses. The sub-grid scale stresses represent the contribution of the small unresolved scales to the large resolved ones. These are unknown and must be modeled. The Smagorinsky model is used in the present work to model the SGS stresses because of its simplicity and in order to reduce computational cost. It models the SGS stresses as:

$$\tau_{ij} - \frac{1}{3}\delta_{ij}\tau_{kk} = -2\nu_{sgs}\bar{S}_{ij} \tag{2.3}$$

where $\bar{S}_{ij}$ is the resolved rate of strain defined as:

$$\bar{S}_{ij} = \frac{1}{2}\left(\frac{\partial \bar{u}_i}{\partial x_j} + \frac{\partial \bar{u}_j}{\partial x_i}\right) \tag{2.4}$$

and ν_{sgs} is the SGS viscosity defined as:

$$\nu_{sgs} = (C_s f \Delta)^2 \mid \bar{S} \mid . \tag{2.5}$$

Here, $\mid \bar{S} \mid = (2\bar{S}_{ij}\bar{S}_{ij})^{1/2}$, C_s is the SGS model coefficient and f is the van Driest damping function that has the form:

$$f = 1 - exp\left(\frac{y^+}{25}\right). \tag{2.6}$$

The value of the SGS model coefficient, C_s, is 0.1 in the present work. Since the resolved strain-rate tensor, $\bar{S}_{ij}$, does not vanish at the wall, the value of the coefficient, C_s, should be adjusted to take partially into account the effect of the wall. Thus, the damping function, f, is used to damp the turbulence length-scale next to the wall. The same model constant has been used in simulations of the flow around simplified road vehicles [16, 17]. The filter width, Δ, is taken as the cubic root of the volume of a finite volume cell.

2.2 Numerical implementations

Two computations on two different computational grids were made for each model at each yaw angle in order to investigate the influence of the mesh resolution on the results and to establish numerical accuracy. The ICEM-CFD commercial grid-generator package was used to create the meshes. In this work, the numerical flow predictions were carried out using an in-house finite volume developed multi-purpose package CALC-PVM for parallel computations of turbulent flow in complex multi-block domains. LES equations were discretized using a three-dimensional finite volume method in a collocated grid arrangement using Rhie-Chow interpolation. The convective, viscous diffusion plus sub-grid fluxes were approximated by second-order-accurate central difference scheme. To reduce the numerical dissipation, no upwind schemes were used in the simulations. Because of that, the mesh stretching ratio was kept below 1.1 around the train models since the central difference scheme is more sensitive to the stretching ratio, especially in the places where large flow variations are expected (close to the train model and in the wake where the flow is highly unsteady). The time integration was done using the Crank-Nicolson second-order scheme. The SIMPLEC algorithm was used for the pressure-velocity coupling. Additional details about this code can be found in [18].

2.3 Boundary Conditions

Three simulations were made in this work. Two simulations use a generic train model while the third simulation uses a simplified ICE2 train. In all the simulations, the train used is stationary without wheels or suspension so that the train can not move with the wind. The models and yaw angles in our study are those for which experimental data are available. The computational domains are similar to the experimental set-up in all simulations. The flow enters the computational domain with the uniform velocity profile being constant in time. The domain is extended upstream a sufficient distance from the model to ensure constant inlet total pressure and to allow the generation of some turbulence in the flow before it approaches the model. The exit plane is also extended downstream of the model to allow proper shedding in the wake and to use a convective boundary condition at the exit. The meshes are concentrated around the model and ground board in order to resolve the important near-wall flow structures. No-slip boundary conditions are applied on the train wall and the floor. The boundary conditions on the side walls and roof are set depending on the exper-

imental set-up. For open wind tunnel, slip boundary conditions are used on the side walls and roof while wall functions are used for the closed wind tunnel. For all cases, a homogeneous Neumann boundary condition is used for the pressure on all the boundaries.

Chapter 3

Visualization Techniques

The first step in the analysis of the LES results is to visualize the flow around the train. This step is very important for understanding the flow structure and highlighting the flow spots that are of special features. Streamlines, path lines, separation and reattachment lines are tools commonly used to visualize the time-averaged surface flow. Different tools (such as local minimum pressure and second invariant of velocity gradient) are used to define the vortex cores in the wake and around the vehicle in both the instantaneous and time-averaged flows. Ensight package for flow visualization is used to visualize the three-dimensional data where most of the flow visualization tools are implemented. The following sections give a short description of the visualization tools used in this work.

3.1 Second Order Tensor Characteristics

The tensor can be defined as a linear transformation of vectors [19]. According to this definition, if a vector a_j is transformed to another vector b_i through a linear transformer A_{ij} as in Eq. 3.1,

$$A_{ij}a_j = b_i \tag{3.1}$$

then A_{ij} is a tensor.

3.1.1 Rotation Tensor

The rotation tensor is a tensor that transforms vectors in a rigid body rotation manner. That is, the rotation transforms vectors drawn in the rigid body into other vectors. Consequently, there is an infinite number of rotation tensors according to the angle that they rotate the vectors.

3.1.2 Eigenvalues and Eigenvectors of a Tensor

If there is a vector a_j that transforms under a tensor A_{ij} to a vector parallel to itself, i.e.

$$A_{ij}a_j = \lambda a_i, \tag{3.2}$$

then vector a_i is called the eigenvector of the tensor A_{ij} and the constant, λ, is the corresponding eigenvalue. The eigenvector components can be determined in an automatic way if we rearrange Eq. 3.2 to be written in the following form

$$(A_{ij} - \lambda\delta_{ij})a_j = 0. \tag{3.3}$$

Equation 3.3 is a system of linear homogeneous algebraic equations in a_1, a_2, and a_3. Obviously, regardless of the values of λ, a solution of this system is $a_1 = a_2 = a_3 = 0$. This is known as the trivial solution. This solution simply states the obvious fact that $a_j = 0$ satisfies the equation $A_{ij}a_j = \lambda a_i$, independent of the value of λ. To find the nontrivial eigenvectors for A_{ij}, we note that a homogeneous system of equations admits nontrivial solution only if the determinant of its coefficients vanishes. That is

$$\begin{vmatrix} A_{11} - \lambda & A_{12} & A_{13} \\ A_{21} & A_{22} - \lambda & A_{23} \\ A_{31} & A_{32} & A_{33} - \lambda \end{vmatrix} = 0. \tag{3.4}$$

The above equation is a cubic equation in λ. It is called the characteristic equation of tensor A_{ij}. The roots of this characteristic equation are the eigenvalues of A_{ij}. The eigenvectors can be calculated from equation 3.3 using the eigenvalues that have been calculated from Eq. 3.4.

If tensor A_{ij} is symmetric, then the three eigenvalues λ_1, λ_2 and λ_3 are real. This gives three real eigenvectors to tensor A_{ij} corresponding to the three real eigenvalues. On the other side, some tensors have eigenvectors in only one direction. For example, for any rotational tensor that affects a rigid body rotation about an axis, only those vectors that are parallel to the axis of rotation will remain parallel to themselves. In general, the antisymmetric real tensors, which have real components like the rotational tensor, have two complex conjugates eigenvalues and one real. The real eigenvalue gives one real eigenvector that is parallel to the axis of rotation.

3.1.3 Principal Invariants of a Tensor

The characteristic equation 3.4 can be written as

$$\lambda^3 - P\lambda^2 + Q\lambda - R = 0 \tag{3.5}$$

where

$$\begin{aligned} P &= trA_{ij} \\ Q &= \tfrac{1}{2}(A_{ii}A_{jj} - A_{ij}A_{ji}) = \tfrac{1}{2}[(trA_{ij})^2 - tr({A_{ij}}^2)] \\ R &= det[A_{ij}]. \end{aligned} \tag{3.6}$$

Since by definition the eigenvalues of tensor A_{ij} do not depend on the base vectors, the coefficients of Eq. 3.5 will not depend on any particular choice of basis. They are called the principal invariants of tensor A_{ij}.

3.2 Critical Point Theory

It was and is still difficult to visualize the flow field in three-dimensional data sets. This is because turbulent flows are characterized by vortices ranging in size from the integral length scale down to the Kolmogorov scale, and the definition of the vortex is still unclear.

Most of the proposed definitions of vortices are based on the critical point theory. The critical points are points in the flow field where the streamline slope is indeterminate and the velocity is zero relative to an appropriate observer. Asymptotically exact solutions of Navier-Stokes and continuity equation were found close to the critical points, as in the work of Perry and Chong [20]. These solutions give a number of standard flow patterns close to the critical point.

One of the most important parts of the flow visualization is to determine the critical points in both of the instantaneous and the time-averaged flow. In the three-dimensional numerical solution of Navier-Stokes equations, the solution domain is divided to very small cells that may take different shapes. One of these common shapes in computational fluid dynamics is the hexahedral cell, which is commonly used in the structured mesh in the finite volume method. The critical points are found in the cells where the u, v and w components of the velocity vector pass through zero. Taylor series can be used to expand velocity u_i around any arbitrary point, O, inside the cell. This gives

$$u_i = A_i + A_{ij}dx_j + A_{ijk}dx_jdx_k + \ldots\ldots \tag{3.7}$$

Coefficients A_i, A_{ij} etc. are functions of time if the flow is unsteady, and they are symmetric tensors in all indices except the first. If O is located at a critical point, then A_i are equal to zero since the velocity is zero at the critical point relative to an appropriate observer. Moreover, since the cell is very small and infinitesimal, then Eq. 3.7 can be truncated at the first-order term. The higher order terms have very little

influence in Eq. 3.7 only if the cell size is large. Since we are dealing here with infinitesimal cells, we can use the truncated equation as an exact expression for the velocity field inside the cell. This gives

$$\left.\begin{array}{l} u \approx \frac{\partial u}{\partial x}dx + \frac{\partial u}{\partial y}dy + \frac{\partial u}{\partial z}dz \\ v \approx \frac{\partial v}{\partial x}dx + \frac{\partial v}{\partial y}dy + \frac{\partial v}{\partial z}dz \\ w \approx \frac{\partial w}{\partial x}dx + \frac{\partial w}{\partial y}dy + \frac{\partial w}{\partial z}dz \end{array}\right\}. \tag{3.8}$$

Equation 3.8 can be written in the tensor form as

$$u_i = J_{ij}dx_j \tag{3.9}$$

where J_{ij} is the rate of deformation tensor or velocity gradient tensor, $\partial u_i/\partial x_j$ (Jacobian). The velocity gradient tensor, $u_{i,j}$, can be decomposed into a symmetric part and an antisymmetric part as follows:

$$u_{i,j} = \frac{1}{2}[(u_{i,j} + u_{j,i}) + (u_{i,j} - u_{j,i})]. \tag{3.10}$$

Equation 3.10 can be written as

$$u_{i,j} = S_{ij} + \Omega_{ij} \tag{3.11}$$

where S_{ij} is the symmetric part representing the strain rate tensor, i.e.

$$S_{ij} = \frac{1}{2}(u_{i,j} + u_{j,i}) \tag{3.12}$$

and Ω_{ij} is the antisymmetric part representing the rotation or the spin tensor

$$\Omega_{ij} = \frac{1}{2}(u_{i,j} - u_{j,i}). \tag{3.13}$$

It has been proven that the relative velocity, v_i, can be related to the relative position, dx_j, by an antisymmetric tensor, Ω_{ij}. Thus $v_i = \Omega_{ij}dx_j$ represents a rigid body rotation with an angular velocity of ω [21]

Thus the antisymmetric part of the velocity gradient tensor corresponds to rigid body rotation, and, if the motion is a rigid one, the symmetric part of the velocity gradient tensor will vanish. For this reason, tensor S_{ij} is called the rate of strain tensor and its vanishing is necessary and sufficient for the motion to be without deformation, that is, rigid. It should be remembered that the rotation tensor has one real and two complex conjugate eigenvalues.

At the critical point, if the rotation tensor dominates over the rate of strain tensor, then the velocity gradient tensor, $\partial u_i/\partial x_j$, is an antisymmetric tensor. This implies that one of the eigenvalues is real and the other two are complex conjugates. Thus, an attracting spiral-saddle pattern is formed. Equation 3.9 supports this theory, since the velocity, u_i, rotates around an axis parallel to the real eigenvector, which corresponds to the real eigenvalue. If the real eigenvalue is zero, then the critical point has absolute zero velocity. Otherwise it moves in the direction of the real eigenvector with a velocity equal to the real eigenvalue. The flow pattern around the critical point in that case is called focus. On the other side, if the eigenvalues and eigenvectors of the velocity gradient tensor, $\partial u_i/\partial x_j$, are real, then three planes can be defined by the eigenvectors, and this will be referred as the eigenvector planes. These planes do not need to be mutually orthogonal and, in general, they are the only planes that contain solution trajectories (i.e. some of the streamlines oscillate to these planes close to the critical points). Figure 3.1 shows the different kinds of critical points that can appear in the flow.

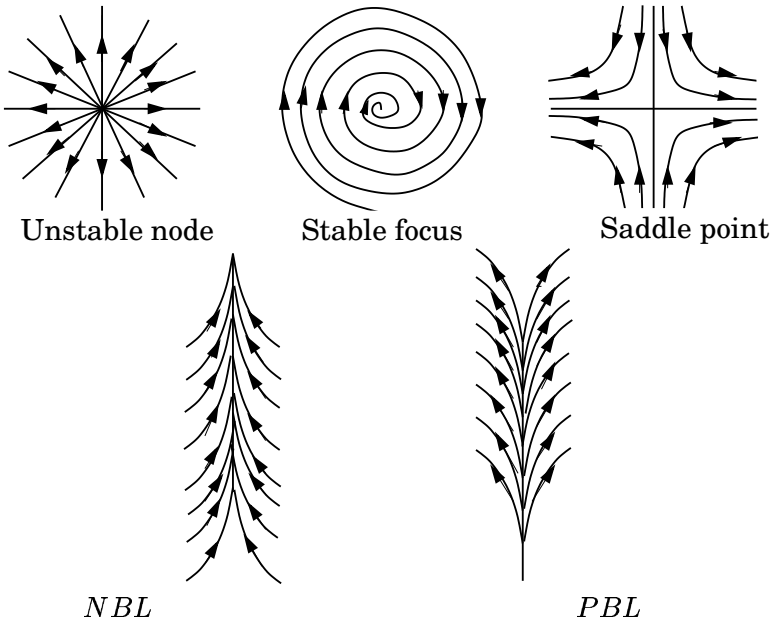

Figure 3.1: Schematic representation of an unstable node, stable focus and saddle. NBL and PBL are negative and positive bifurcation lines, respectively.

3.3 Streamlines and Path-lines

Streamlines and path-lines are useful tools for visualizing the flow, especially on the model surface, since the separation and reattachment lines can easily be detected. Vortex can be also detected using streamlines as each pair of separation and reattachment lines has an associated vortex core. Streamlines can, together with velocity vectors projected on the surface, be used to identify critical points. However, there is a problem in terms of of predicting the critical points in the time-averaged three-dimensional data sets far from the surface since the streamlines are not Galilean invariant.

3.4 Vortex Core

Since the turbulence is viewed as a tangle of vortex filaments and most of turbulence physics is well explained using the concept of vortex dynamics, a definition of a vortex could be used for flow visualization. Although the concept of a vortex is very old, we still lake a definition of it. As a consequence, different vortex definitions are proposed in the literature. Jeong and Hussain [22] summarized the different definitions for vortex core and proposed a new definition based on the following requirements:
(1) The vortex core must have net vorticity.
(2) It should be Galilean invariant.
They found that the intuitive indicators of vortices such as local pressure minimum, closed or spiraling streamlines and path-lines, and isovorticity surface are inadequate and not suitable tools for detecting vortices in an unsteady flow.

3.4.1 Region of Constant Vorticity Magnitude

Vorticity magnitude (ω) has been widely used to educe coherent structure and represent vortex cores [22]. However, this approach is not always satisfactory since $\mid \omega \mid$ does not identify vortex cores in shear flow, especially if the background shear is comparable to the vorticity magnitude within the vortex. Thus, a $\mid \omega \mid$ at a sufficiently low level is necessary but not sufficient to detect a vortex in both free and wall-bounded free shear flows [22].

3.4.2 Region of Complex Eigenvalues of Velocity Gradient Tensor

The critical point theory can be used to identify the center of the swirling flow (i.e. vortex core). According to the theory, the eigenvalues and eigenvectors of the rate of deformation tensor, $\partial u_i/\partial x_j$, evaluated at the critical point define the flow pattern about that point. Specifically, if the eigensystem displays one real and one pair of complex-conjugate eigenvalues, the flow forms a spiral-saddle pattern. The two eigenvectors corresponding to the pair of complex-conjugate eigenvalues define the plane on which the flow swirls, while the eigenvector corresponding to the real eigenvalue points in the direction about which the flow spirals. The eigenvalues, λ, of the velocity gradient tensor, $u_{i,j}$, satisfy the characteristic equation Eq. 3.5 where

$$\begin{aligned} P &= u_{i,i} = 0 \\ Q &= \tfrac{1}{2}[(u_{i,i})^2 - u_{i,j}u_{j,i}] \\ R &= det[u_{i,j}] \end{aligned} \tag{3.14}$$

are the three invariants of $u_{i,j}$. The vortex core can be defined as the region of complex λ that will occur when the discriminant, Δ, of Eq. 3.5 is positive, i.e.

$$\Delta = (\frac{1}{3}Q)^3 + (\frac{1}{2}R)^2 > 0. \tag{3.15}$$

The above criteria have been used by Sujudi and Haimes [23] to develop an algorithm to automatically locate the center of the swirling flow in a three-dimensional vector field. The algorithm uses only tetrahedral cells, with all other cell types reduced to two or more tetrahedrals. It evaluates the velocity distribution inside the cell using linear interpolation of four node points of the tetrahedral in the form:

$$u_i = c_i + \frac{\partial u_i}{\partial x_j}\Delta x_j. \tag{3.16}$$

The rate of deformation tensor is simply the coefficient of the linear interpolation velocity vector. The algorithm checks the eigenvalues for each tetrahedral cell in the computational domain. If there is a cell where one real and a pair of complex conjugate eigenvalues for the rate of deformation tensor are found, then a vortex core passes through it.

3.4.3 Region of Positive Second Invariant of Velocity Gradient

The second invariant of the velocity gradient, Q, is defined in Eq. 3.14 as

$$Q = \frac{1}{2}\left[(u_{i,i})^2 - u_{i,j}u_{j,i}\right]. \tag{3.17}$$

For incompressible flow, $u_{i,i} = 0$, this gives

$$Q = -\frac{1}{2}u_{i,j}u_{j,i} = \frac{1}{2}\left(\|\Omega\|^2 - \|S\|^2\right) \tag{3.18}$$

where $\|S\| = \left[tr\left(S_{ij}{S_{ij}}^t\right)\right]$, $\|\Omega\| = \left[tr\left(\Omega_{ij}{\Omega_{ij}}^t\right)\right]$ and S_{ij} and Ω_{ij} are the symmetric and antisymmetric components of the velocity gradients as defined in Eq. 3.12 and Eq. 3.13, respectively. Thus Q represents the local balance between the shear strain rate and vorticity magnitude. The region of positive Q implies that the rotation tensor dominates over the rate of strain tensor, i.e. there is a vortex. Moreover, from Eq. 3.15, positive Q implies positive Δ, i.e. the condition of $Q > 0$ is more restrictive than $\Delta > 0$.

3.4.4 Region of Negative λ_2

Jeong and Hussain [22] proposed a new definition of the vortex core based on the local pressure minimum after discarding the viscous effect that can eliminate the local pressure minimum in a flow with vortical motion and also the effect of the unsteady straining, which can create pressure minimum without involving vortical or swirling motion. Using the above criteria, they defined the vortex as the region of the flow that has two negative eigenvalues for tensor ${S_{ij}}^2 + {\Omega_{ij}}^2$. If λ_1, λ_2 and λ_3 are the eigenvalues and $\lambda_1 \geq \lambda_2 \geq \lambda_3$, the definition is equivalent to the requirement that $\lambda_2 < 0$ within the vortex core.

3.4.5 Region of Minimum Local Pressure

The pressure will have a local minimum in the vortex core in the case in which the centrifugal force is balanced by the pressure force. In that case, the local pressure isosurface can be used to identify the vortex core. Unfortunately, in some cases the centrifugal force can be balanced by the viscous force. This will imply that the method in this case fails to identify the vortex. Thus, the existence of a local pressure minimum is neither a sufficient nor a necessary condition for the presence of a vortex core in general [22].

Chapter 4

Side-Wind Flow over a Simplified ICE2 Train Model

This chapter investigates the flow around a simplified high-speed train model of the Inter-City Express 2 (ICE2) under a side wind using LES. The study is restricted to a side-wind yaw angle of 30^o and Reynolds number of 2×10^5 based on the free-stream velocity and height of the train.

4.1 Train model and computational domain

The simplified train model consists of a leading car to which an end car dummy is attached. The total length of the train model is $L = 3.552m$ and its height is $D = 0.358m$. These dimensions are 1:10 of the real dimensions of the leading train car. The clearance between the train and the computational domain floor is $0.0537m$ $(0.15D)$. The model is shown in Fig. 4.1.

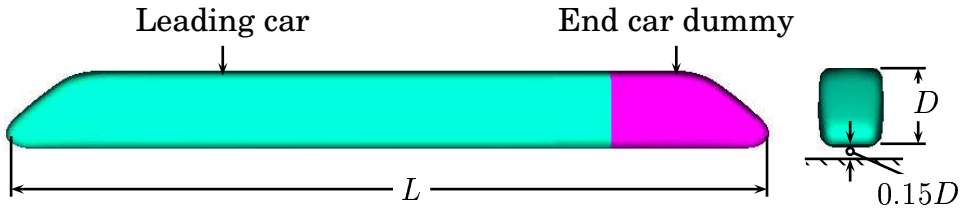

Figure 4.1: Computational ICE2 train model

The LES results are compared with wind tunnel test results. The measurements were made in the subsonic Russian $TsAGI$ $T-103$ open jet tunnel. The experimental set-up is shown in Fig. 4.2. In contrast to

the computational model, the wind tunnel model has bogies and an inner gap between the leading car and the dummy end car. Moreover, in order to keep the ground clearance, the model is held by a single cylindrical support positioned midway between the bogies. To simplify the model in the computations, the inner gap is filled and both the bogies and the cylindrical support are removed. In the measurements, the Reynolds number was $Re = 1.4 \times 10^6$ based on the free-stream velocity and the height of the train. A six-component external gauge was used to measure the aerodynamic forces and moments on the train. The time-averaged data were collected in $4sec$ with a sampling frequency of $100Hz$ [24]. The model stands on a thin elliptic plate (see Fig. 4.2) to reduce the thickness of the approaching boundary layer.

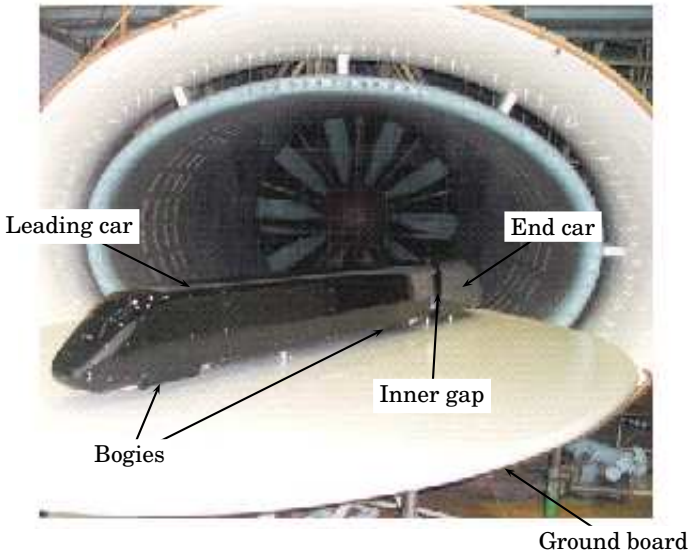

Figure 4.2: Experimental set-up. Taken from [24].

In the computational domain, the model is yawed 30^o to the free-stream direction as shown in Fig. 4.3. The clearance between the model and the ground board is typically the same as in the experimental set-up.

The model centerline is kept parallel to the inlet of the domain with an $8D$ streamwise distance to ensure the same thickness of the approaching boundary layer. The distance between the train tail and the exit of the computational domain is $21D$ downstream. These dimensions proved to be sufficient in a similar work around ground vehicles [16, 17]. The height of the computational domain is $5.2D$.

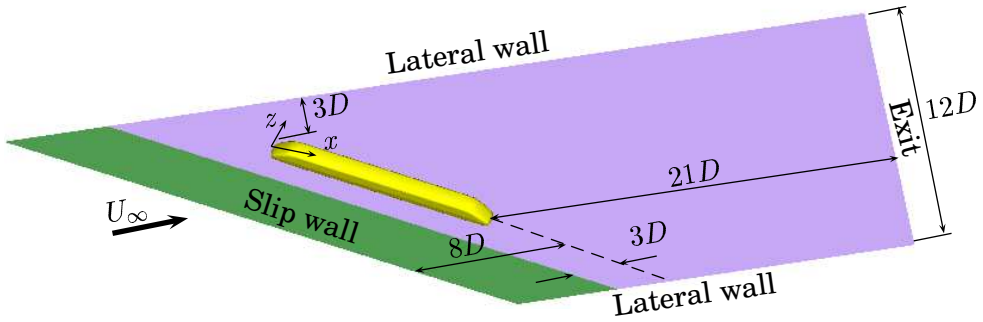

Figure 4.3: Computational domain

4.2 Boundary conditions

The flow enters the domain with a uniform velocity profile constant in time. A convective boundary condition is implemented at the domain exit. No-slip boundary conditions are used on the train surface. To simulate the experimental set-up, a slip boundary condition is applied at the lateral walls and the roof. To reduce the thickness of the boundary layer approaching the train model, two kinds of boundary conditions are applied at the channel floor. A slip boundary condition is applied on a part extending $5D$ (see Fig. 4.3) from the inlet to suppress the development of a boundary layer, while a no-slip boundary condition is used on the rest of the floor. A homogeneous Neumann boundary condition is used for the pressure on all the boundaries.

4.3 Numerical details

LES is performed on the previously described model at Reynolds number of 2×10^5 based on the free-stream velocity and height of the train. The ICEM-CFD mesh generator package is employed to build a structured mesh around the train. The total number of nodes in the computational domain is 11 million. Another simulation using a finer mesh (17 million) is ongoing. A dummy ICE2 train is built around the model. The belt of thickness $0.06D$ between the model and the dummy train is used to make an O-type grid. Another O-type grid is built around the first one to give better control of the mesh stretching as shown in Fig. 4.4. The dummy train surface is used as a sheared wall between the two O-type grids. H-type meshes are used in the rest of the grid topology. Figure 4.4.b depicts the mesh density on the train surface and the channel floor.

Hyperbolic stretching is used in the whole domain. The stretching ratio between any two successive cells in the O-type meshes does not

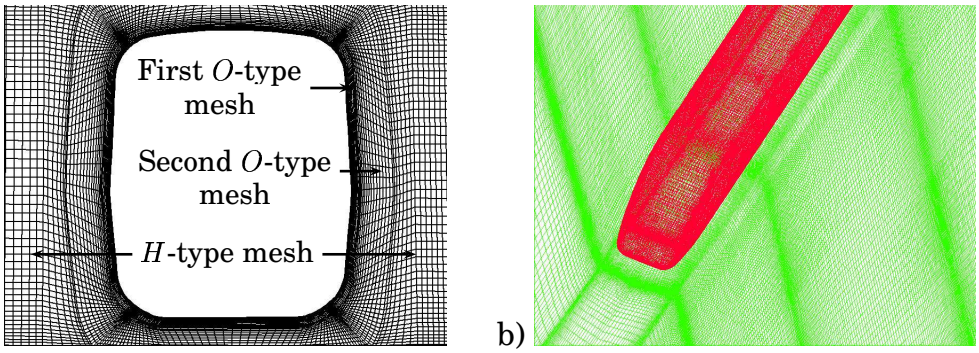

Figure 4.4: Computational mesh around the ICE2 train. (a) Cross-section of the mesh showing the O-type grids. (b) Mesh density on the train surface and the channel floor.

exceed 1.1. This ratio varies in the H-type meshes but is kept below 1.5 in any extreme place in the mesh. To resolve the boundary layer on the model surface and to capture the variation of the flow physics around it, the mesh is concentrated around the model where more than 20% of the total nodes are confined in the O-type grids. The governing equations are solved all the way to the model wall to insure proper variation of the flow quantities in the near-wall region, where much of the flow physics originates. The grid density near the wall was fine enough to resolve the small-scale structures that arise via shear layer instabilities. The spatial resolutions of the first cell layer at the model and floor are shown in Table 4.1, where u^* is the friction velocity, n is the distance between the first node and the train surface in the wall normal direction, Δs is the cell width in the streamwise direction and Δl is the cell width in the span-wise direction.

Table 4.1: Spatial resolutions for the coarse mesh simulation.

	$y^+ = nu^*/\nu$	$s^+ = \Delta s u^*/\nu$	$l^+ = \Delta l u^*/\nu$
mean	0.5	40	90
maximum	4	250	700

LES equations are discretized using the three-dimensional finite volume method in a collocated grid arrangement using Rhie-Chow interpolation. Since the high frequency modes in the model boundary and shear layers are important in side-wind simulations, the viscous diffusion and sub-grid fluxes are approximated by a second-order-accurate

central difference scheme. It was not possible to use pure central difference discretization for the convective flux because of divergence problems. Instead, the convective flux is approximated using a blend of a 10% second-order upwind scheme (Van-Leer) and a 90% second-order central difference scheme. The numerical dissipation that gained from the 10% upwind scheme played an important role in the stabilizing of the convergence. The time integration is done using the Crank-Nicolson second-order scheme. The SIMPLEC algorithm is used for the pressure-velocity coupling. Fully developed turbulent flow is obtained from the simulation after time $t^* = tU_\infty/D = 170$. The physical time step is 1.0×10^{-4} ($t^* = 0.0008$), which gives a maximum Courant-Friedrichs-Levy CFL number of about 1.5. The time-averaged flow is obtained using $t^* = 28$, which is about two and half times longer than the experimental sampling time.

4.4 Results

The choice of the proper boundary conditions is crucial in any numerical simulation. Since the inlet boundary condition is a uniform velocity profile constant in time, the distance between the inlet plane and the model surface should be long enough to avoid the influence of the model on the inlet total pressure. This distance is also necessary to get some turbulence in the flow before it approaches the model as an attempt to simulate the natural wind. Moreover, the slip boundary conditions that are used on the lateral walls and roof of the channel require a sufficient distance from the model to be applicable.

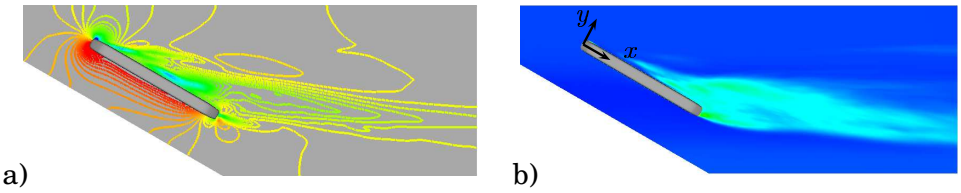

a) b)

Figure 4.5: Cross-section of the computational domain at the middle of the train, parallel to channel floor: (a)showing static pressure contours, (b) colored by total pressure.

Thus attention is paid to the size of the numerical domain and the the position of the model inside it. In order to reduce the total number of nodes and to get high resolution, which is required for good LES, the size of the computational domain should be as small as possible. This is

met by the blocking constraint and the requirement of a constant total pressure at the inlet and lateral walls. The influence of the model on the static and total pressures of the boundaries are shown in Fig. 4.5. Figure 4.5.a represents the static pressure contours on a plane parallel to the channel floor at the middle of the height of the train, where the distance between the inlet plane and the train surface is at its minimum. There are variations in the static pressure on the boundaries of the computational domain. Figure 4.5.b displays the same plane colored by the time-averaged total pressure. The total pressure at the inlet and lateral walls is approximately constant and is not affected by the model. There is a total pressure loss in the wake behind the train. This loss extends to the exit of the channel.

4.4.1 Time-averaged flow

The physical time step in our LES computation is $\Delta t = 0.0001$ sec. The time-averaged data are collected using 100000 time steps. This corresponds to a simulation time of $10sec$ ($t^* = 28$), which is 2.5 times longer than the sampling period in the wind tunnel measurements. These data are used to calculate the statistics of the flow and to explore the flow structures around the train in the time-averaged sense. In this section, the surface pressure distribution is computed and compared with the measured surface pressure. The wake structures and their influences on the surface flow pattern are explored.

Surface pressure distribution

The surface pressure distributions are computed at certain cross-sections along the length of the train where experimental data are available, as shown in Fig. 4.6. Figure 4.6 also shows some details from the experimental train, such as spoiler, support, bogies and inner-car gap, which are omitted from the computational model. These differences should be kept in mind when comparing the LES results with the experimental data. Figure 4.7 displays the local pressure coefficient, C_p, distributions over the circumferential angle, θ, measured counterclockwise around the x-axis, as shown in Fig. 4.6. The LES results show good agreement with the measurements on the streamwise and topside faces at all the cross-sections. Moreover, good correlation is obtained between the LES results and the measured data on the lee-side face. The difference in the geometry under the train (i.e. bogies, the spoiler and the support) between the experimental and the numerical set-ups resulted in a difference in C_p values on the surface of the under side.

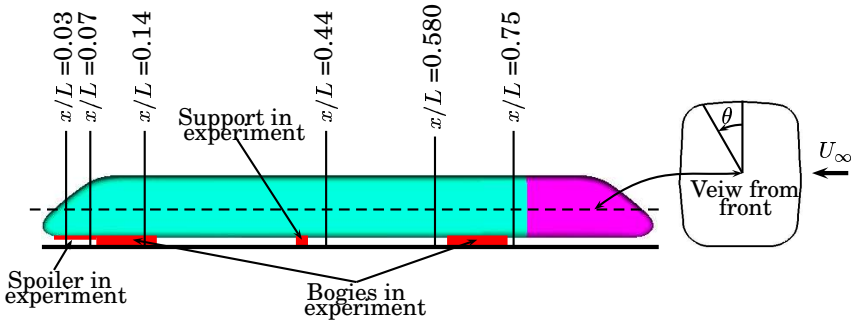

Figure 4.6: Location of the measured time-averaged pressure distributions and the orientation of angle θ.

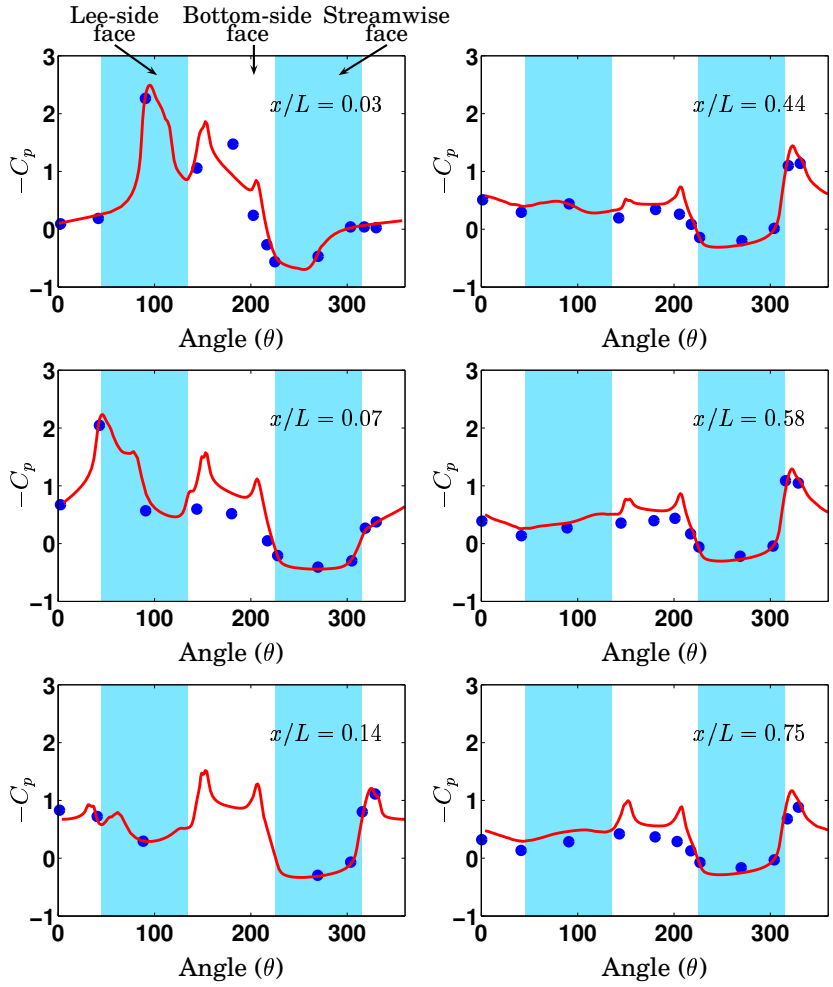

Figure 4.7: Comparison of the surface pressure coefficient distribution along the length of the train: LES (solid line); experimental data from [24] (symbols).

Suction pressure is reported in the experimental data at the most frontal position, $x/L = 0.03$, on the bottom side of the train. This suction pressure can be attributed to the influence of the front spoiler. The influence of the bogies is shown as higher C_p values at the streamwise corner on the underbody face at $x/L = 0.07$. There are no measured data on the underbody face at $x/L = 0.14$ due to the existence of the bogies. The LES results coincide with the measured data at the other faces at that position. Cross-section $x/L = 0.44$ is probably the best one for a comparison between our LES results and the experimental data since it is the position farthest from the bogies. Although the influence of the bogies on the flow at this position is relatively small, the flow is also affected by the support cylinder. However, there is good agreement between the LES results and the measurements on all the faces. Farther from the train front, at $x/L = 0.58$ and 0.75, the influence of the underbody details (bogies, the support and the spoiler) used in the experiment are still visible. In addition, the influence of the inner-car gap appears on the lee-side face pressure distribution, where measured C_p values are higher than LES results. The maximum suction peak and the highest pressure are found on the upper-face leeward edge of the nose and on the streamwise face of the nose, respectively, at two front cross-sections, $x/L = 0.03$ and $x/L = 0.07$ (Fig. 4.7). The peak C_p magnitudes in these two sections are almost twice as large as those in the subsequent cross-sections. This suggests that the loads are accumulated in the nose region of the leading car and increase the importance of the nose shape in the side wind instability. In general, although the LES Reynolds number is seven times lower than the experimental one, the LES results are in fairly good agreement with the measurements.

Surface flow patterns

Figure 4.8 displays the LES streamlines projected on the train surface representing the time-averaged surface flow patterns. The surface flow pattern displays regions of separated and attached flow. These regions are separated by separation, reattachment and bifurcation lines. Figure 4.9 is a schematic representation of these lines as inferred from Fig. 4.8. Figure 4.8.a shows a uniform flow over the streamwise face. There is one bifurcation line, B_1, on the streamwise face, as shown in Fig. 4.9.a, from which flow is moving toward the roof and the bottom of the train. As soon as the flow reaches the upper-side face it separates from the face at separation line S_1, as shown in Fig. 4.9.b. The Reynolds number in the simulation is 2×10^5, which is about 30 times lower than the Reynolds number of the real high-speed trains at the normal operating conditions. Thus separated flow is expected on the

upper-side face. The flow attaches to the face at the reattachment line, A_1, as shown in Fig. 4.9.b. Figure 4.8.b shows that the separated flow on the upper-side face is increasing in the direction of the length of the train. At approximately $x/L = 0.4$, the face is completely covered by the separated flow. The flow separates on the bottom-side face at separation line S_3, and reattaches at reattachment line A_2, forming a small separation bubble in the underbody flow. Both the reattached flow on the upper-side and the bottom-side faces separate from the train surface when they reach the lee-side edge at separation lines S_2 and S_4, respectively. The two vortex sheets shedding from the upper side and under side of the train roll up to form separation bubbles in the wake flow. These bubbles are not always attached to the surface but they detach from the surface at successive places along the length of the train. When these vortices detach from the surface, other vortices are formed. Figure 4.8.c shows a complicated flow pattern on the lee-side face caused by the attachment and detachment of the wake vortices. Figure 4.10 shows part of this flow on the lee-side face of the train nose. The two recirculation bubbles shed from the upper and lower sides of the face and meet at bifurcation line B_2 on the train surface. The attached flow from the upper recirculation bubble moves toward the roof of the train where it separates on secondary separation line S_5 and reattaches to the surface at secondary reattachment line A_3 before it separates again at primary separation line S_2. Similarly, the attached flow from the floor-side recirculation bubble moves toward the bottom-side face. Figure 4.10.b shows that this flow separates from the train surface at secondary separation line S_6 and reattaches to the surface at secondary reattachment line A_4 before it separates again at primary separation line S_4. The size of the recirculation bubbles increases in the positive x-direction along the train. After a certain distance, they have completely detached from the face and convected away into the wake flow. Once these two circulation bubbles detach from the train surface, two other bubbles are formed. This process is repeated along the the length of the train with bifurcation lines B_3 and B_4 and secondary separation lines S_7 and S_8 for the lower recirculation region, as shown in Fig. 4.9.c. On the other side, the upper recirculation region seems to be attached to the train surface for approximately two-thirds of the length of the train, as is shown by long secondary separation and reattachment lines S_5 and A_3, respectively.

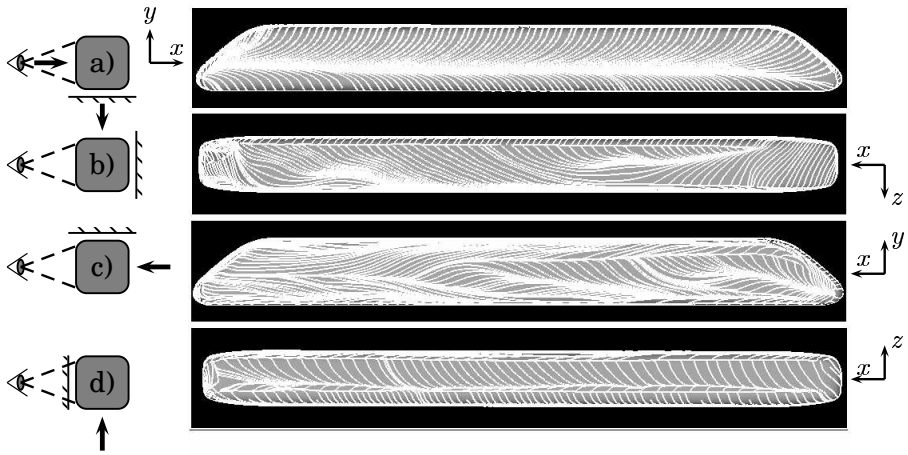

Figure 4.8: Time-averaged trace lines projected on the surface of the train showing surface flow patterns.

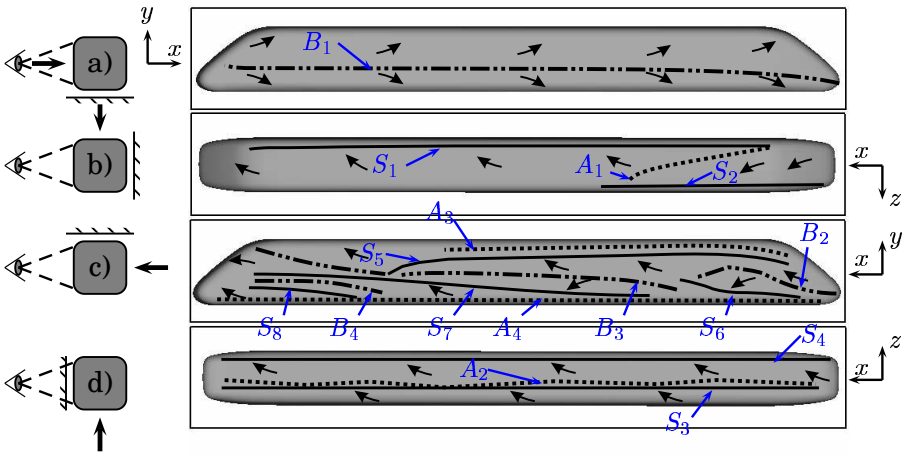

Figure 4.9: Schematic representation of the separation and reattachment lines found in Fig. 4.8.

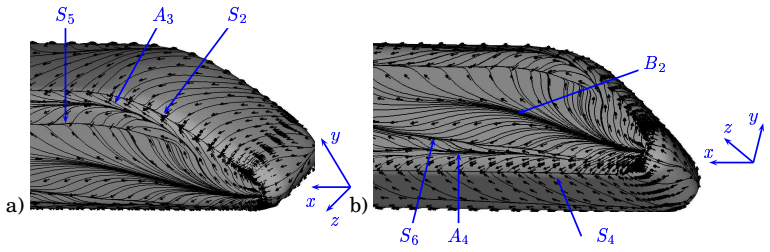

Figure 4.10: Surface flow pattern on the lee-side face of the nose: (a) view from above and the lateral side on the rear end of the train, (b) view from below and the lateral side on the rear end of the train.

Wake structure

Figure 4.11 shows the time-averaged wake structures by means of the vortex cores. Two vortices, Vc_1 and Vc_2, originate on the train nose tip. Figure 4.11.a shows that vortex Vc_1 stretches in the wake flow all the way from the nose tip to the end of the leading car. It grows in size but remains attached to the train surface. Numerous vortices,

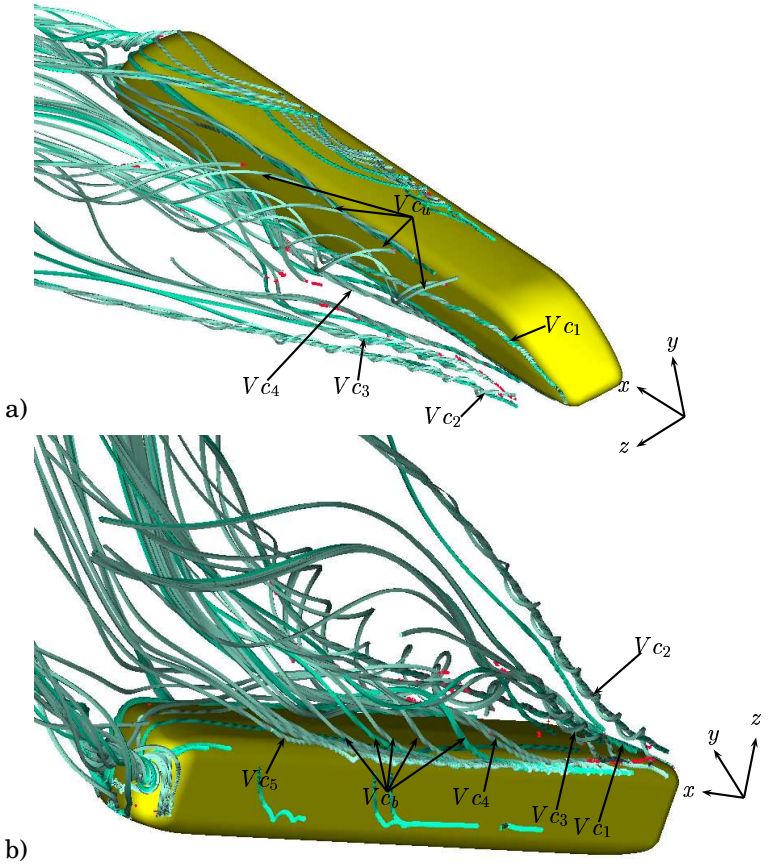

Figure 4.11: Streamlines generated from the vortex cores: (a) view from above, (b) view from below the train.

Vc_u, are born on the lee-side of the upper edge of the train. These weak vortices roll up and merge with the strong vortex, Vc_1. The recirculated flow around the strong vortex, Vc_1, is attached to the upper half of the lee-side face of the train along the length of the leading car until it separates at separation line S_5, as shown in Fig. 4.9.c. In contrast, Fig. 4.11.b shows that the other nose vortex, Vc_2, once it is born on the lower part of the train nose, detaches from the surface and is convected downstream in the wake. At $x/D \approx 1$ another vortex, Vc_3, sheds from the underbody flow. It rolls up and detaches shortly after its onset and

convects downstream in the wake flow. Similarly, another strong vortex, Vc_4, emerges from the lee-side underbody edge. The vortex grows in size in the direction of the length of the train due to the emergence of the other weak vortices, Vc_b, which are born at the same edge. After a short distance in the direction of the length of the train, the vortex Vc_4 detaches from the train surface and changes its direction toward the wake. The process of shedding vortices under the train body continues by shedding vortex Vc_5, as shown in Fig. 4.11.b.

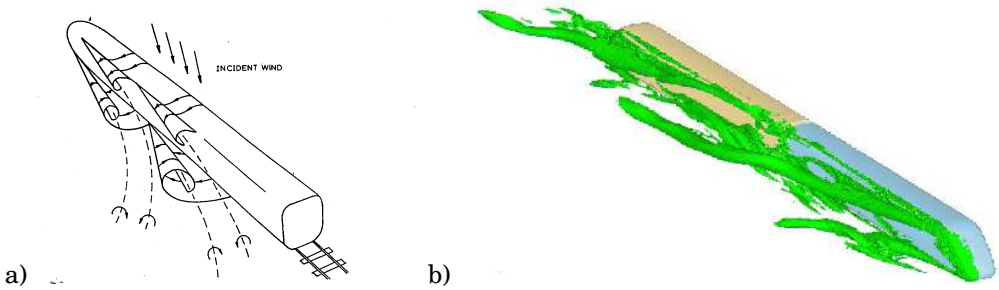

Figure 4.12: Wake structures. (a) Experimental view (taken from [5]). (b) DES results (taken from [24]).

This finding about the wake structures is different from that found in the experimental investigations. Figure 4.12.a shows a schematic representation of the flow around a generic train under the influence of side wind at a 30^o yaw angle by Copley [5]. He defined the wake shedding as a progressive couple of vortices shed from the upper and lower edges of the lee-side face at the same position. Wu [24] computed the flow around the ICE2 model at a 30^o yaw angle using detached-eddy simulation (DES). Although the Reynolds number in his simulation was five times higher (10^6) than that used in the present work, he found in agreement with our results that the upper vortex in the wake flow extends far beyond the inter-car gap, as shown in Fig. 4.12.b. He visualized another vortex shed from the upper edge of the lee-side face directly after the inner-car gap. Besides, he found several vortices that were shed from the underbody. They detach from the surface and decay within a short distance. The model used in his simulation was almost twice as long as in the present work. Thus, the distance that vortex Vc_1 remains attached to the lee-side face is independent of the Reynolds number or the length of the model used in the simulation. Figure 4.13 shows the development of the major vortices in the time-averaged wake flow by means of the pressure minimum. It shows that vortex Vc_1 detaches from the lee-side face after $x/L \approx 0.6$. Along the distance over which Vc_1 remains attached to the surface, a number of

vortices are formed and detach on the lower part of the face.

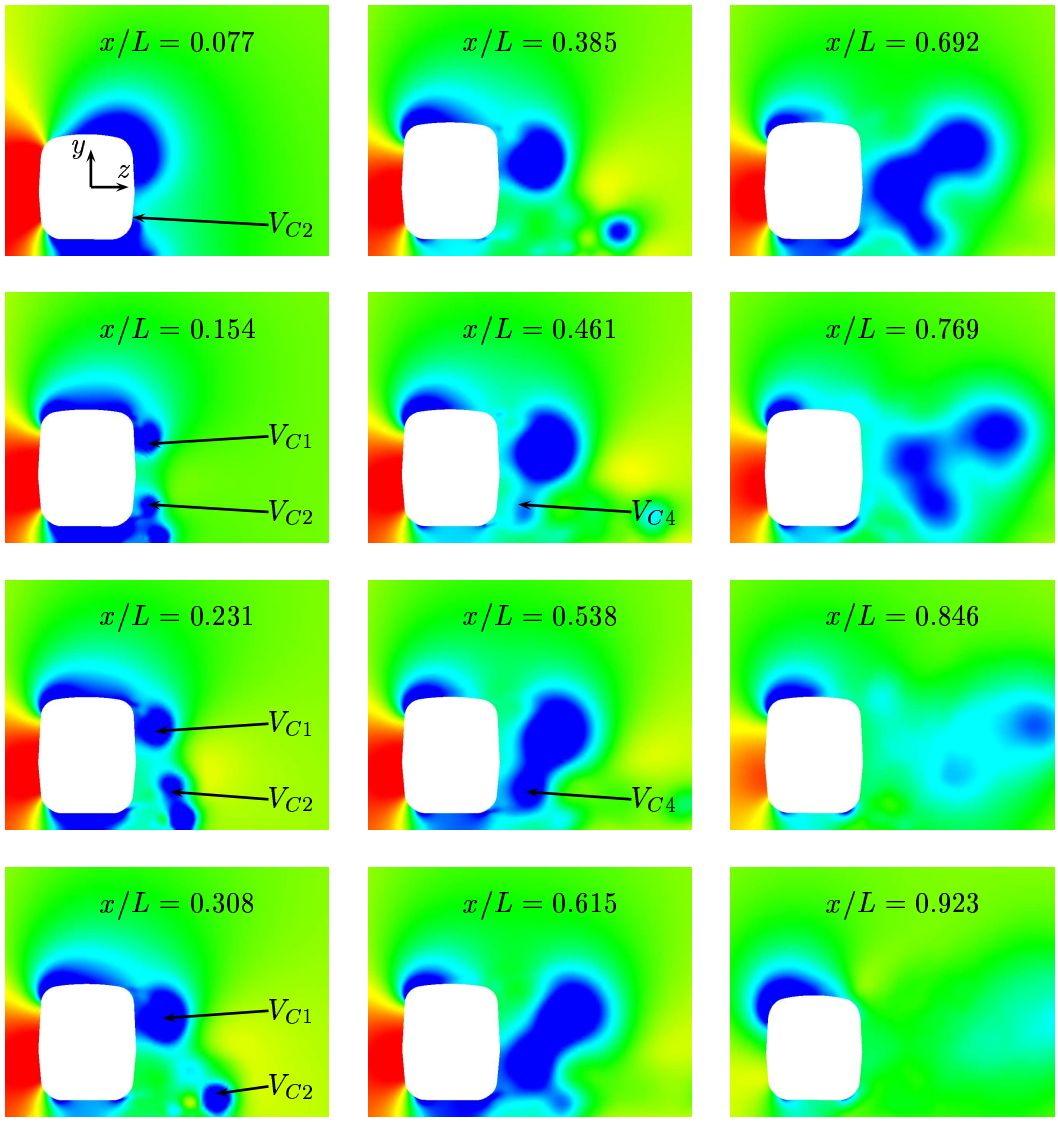

Figure 4.13: Cross-sections colored by the time-averaged static pressure showing the development of wake structures along the length of the train.

4.4.2 Aerodynamic forces

The lift and the side force coefficients are computed at each time step. The values of these coefficients are saved during the averaging process.

The time varying signal is shown in Figs. 4.14.a and 4.14.b for the side and lift coefficients, respectively. Their statistics are shown in Tab. 4.2.

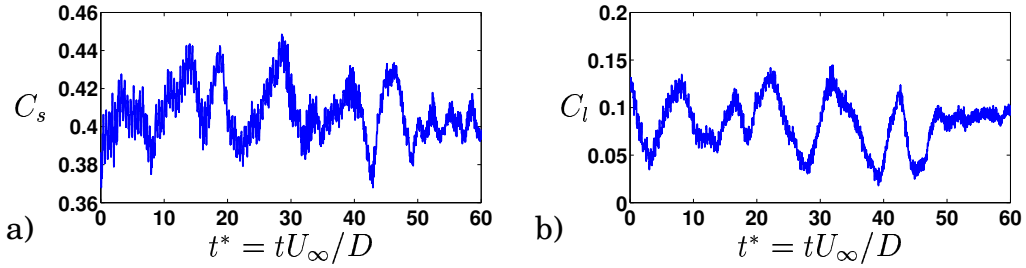

Figure 4.14: Time history of the aerodynamic coefficients. (a) Side force coefficient. (b) Lift force coefficient.

Table 4.2: Statistics of the time varying signal of the aerodynamic coefficients.

force	mean	rms	maximum	minimum
C_s	0.41	0.014	0.449	0.368
C_l	0.0834	0.0257	0.1442	0.0179

Due to the absence of underbody blocking (i.e. bogies, spoiler and support cylinder) in our simplified model, there is relatively high velocity under the train. Consequently, a region with lower pressure exists. This results in a lower mean value of the lift force coefficient $\langle C_l \rangle$ as reported in Tab. 4.2.

4.4.3 Instantaneous flow

The time varying signals of the side and the lift force coefficients reflect the dynamic behavior of the flow around trains at a 30^o yaw angle. Figure 4.14 shows that, in certain time slots, the aerodynamic coefficients oscillate around the mean with high amplitude. These high amplitude oscillations are due to the detachment and reattachment of the wake vortices to and from the lee-side face. The centers of these vortices do not have fixed position in space. Instead, they oscillate in a plane parallel to the channel floor. The higher values of the side force coefficient are associated with the attachment of wake vortices (the nearest distance between the center of the vortices and the lee-side face) and vice versa. This oscillation produces unsteady vortex shedding in the wake.

In contrast to this process, some parts of the time signal of the aerodynamic forces display lower oscillation around the mean. This is because of the stationary behavior of the wake vortices. Only some weak vortex shedding from the upper and lower sides of the train causes the high frequency oscillation of the forces. Here, there is no vortex shedding in the wake flow. Instead, the flow circulates in a spiral way around the stationary vortex cores. This flow is similar to that of the slender body flow.

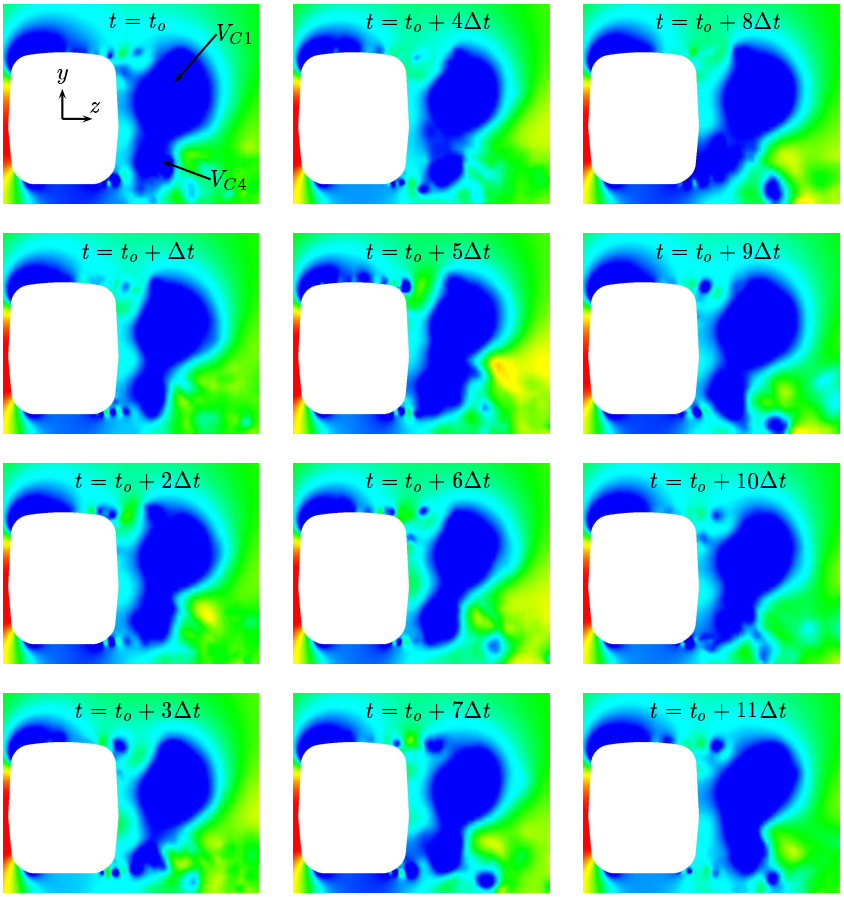

Figure 4.15: Cross-section of the flow at $x/L = 0.538$ colored by instantaneous static pressure. The time difference between two successive snapshot is $\Delta t = 0.1$ sec.

Figure 4.15 gives 12 instantaneous pictures showing the time-varying of the distribution of the local pressure coefficient in the plane $x/L = 0.538$. The plane passes through the major vortices, Vc_1 and Vc_4, and some of the weak vortices, Vc_u and Vc_b. Vortex Vc_1 has different sizes at different times due to the process of merging with the upper weak

vortices. The largest size of vortex Vc_1 is found at time $t = t_o$, yielding low pressure on the upper-side and lee-side faces, shown by the large area of dark color representing the low pressure. Its smallest size is registered at $t = t_o + 6\Delta t$. The center of vortex Vc_1 is fixed in time and space. However, the size of the vortex changes in a regular fashion around the mean size with almost constant frequency. The lower vortices are highly unsteady and their centers are not stationary. At $t = t_o + 8\Delta t$ the vortex is fully attached to the wall, while at $t = t_o + 11\Delta t$ it is fully detached. Figure 4.15 also explores a time-varying size of this vortex. We found that the lower vortices are responsible for the vortex shedding in the wake if it exists and there is no vortex shedding from the upper vortices.

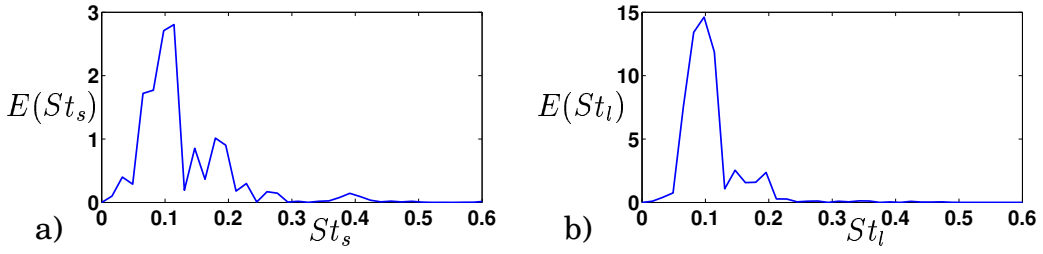

Figure 4.16: Autopower spectra of the time-varying signal of force coefficients. (a) Side force coefficient. (b) Lift force coefficient.

To determine the frequencies of these motions, autopower spectra of the time varying signals of the force coefficient are computed. Figures 4.16.a and 4.16.b show these spectra for side and lift force coefficients, respectively. One common dominating frequency corresponding to $St = 0.1$ is found for both the lift and the side forces. This frequency represents the averaged oscillating frequency of the wake vortices in the horizontal plane. The shedding frequencies are displayed as two other dominating frequencies corresponding to $St = 0.15$ and 0.2. A number of high frequency modes are found in the range of $0.2 < St < 0.4$. These frequencies are caused by the unsteady shedding of the weak vortices from the upper and lower faces of the train.

Bibliography

[1] C.J. Baker. Some complex applications of the wind loading chain. *Journal of Wind Engineering and Industrial Aerodynamics*, 91:1791–1811, 2003.

[2] C.J. Baker, J. Jones, F. Lopez-Calleja, and J. Munday. Measurements of the cross wind forces on trains. *Journal of Wind Engineering and Industrial Aerodynamics*, 92:547–563, 2004.

[3] T. W. Chiu. Prediction of the aerodynamic loads on a railway train in a cross-wind at large yaw angles using an integrated two- and three-dimensional source/vortex panel method. *Journal of Wind Engineering and Industrial Aerodynamics*, 57:19–39, 1995.

[4] T. W. Chiu and L. C. Squire. An experimental study of the flow over a train in a crosswind at large yaw angles up to 90^o. *Journal of Wind Engineering and Industrial Aerodynamics*, 45:47–74, 1992.

[5] J. M. Copley. The three-dimensional flow around railway trains. *Journal of Wind Engineering and Industrial Aerodynamics*, 26:21–52, 1987.

[6] M. Suzuki, K. Tanemoto, and T. Maeda. Aerodynamic characteristics of train/vehicles under cross winds. *Journal of Wind Engineering and Industrial Aerodynamics*, 91:209–218, 2003.

[7] U. Hoppmann, S. Koenig, T. Tielkes, and G. Matschke. A short-term strong wind prediction model for railway application: design and verification. *Journal of Wind Engineering and Industrial Aerodynamics*, 90:1127–1134, 2002.

[8] B. Diedrichs. On computational fluid dynamics modelling of cross-wind effects for high-speed rolling stock. *IMechE*, 217(F):203–226, 2003.

[9] F. Durst W. Khier, M. Breuer. Flow structure around trains under side wind conditions: a numerical study. *Computers & Fluids*, 29:179–195, 2000.

[10] Diedrichs Ben. Computational Methods for Crosswind Stability of Railway Trains. Report, Dept. of Mechanical Engineering, Division of Railway Technology, Royal Institute of Technology, Stokholm, SWEDEN, 2005.

[11] S. Krajnović and L. Davidson. Large eddy simulation of the flow around an Ahmed body. In *2004 ASME Heat Transfer/Fluids Engineering Summer Conference*, Charlotte, North Carolina, USA, 2004.

[12] S. Singh and S. Mittal. Flow past a cylinder: shear layer instability and drag crisis. *Int. J. Num. Meth. Fluids*, 47:75–98, 2005.

[13] G. Kravchenko and P. Moin. Numerical studies of flow over a circular cylinder at Re=3900. *Physics of Fluids*, 12(2):403–417, 2000.

[14] R. Mittal and P. Moin. Stability of upwind-biased finite difference schemes for large-eddy simulation of turbulent flows. *AIAA Journal*, 35(8):1415–1417, 1997.

[15] G.S. Constantinuescu and K.D. Squires. LES and DES investigations of turbulent flow over a sphere at Re=10,000. *Journal of Flow, Turbulence and Combustion*, 70:267–298, 2003.

[16] S. Krajnović and L. Davidson. Flow around a simplified car, part 1: Large-eddy simulation. *ASME: Journal of Fluids Engineering*, 127:907–918, 2005.

[17] S. Krajnović and L. Davidson. Flow around a simplified car, part 2: Understanding the flow. *ASME: Journal of Fluids Engineering*, 127:919–928, 2005.

[18] H. Nilsson and L. Davidson. CALC-PVM: A parallel multiblock SIMPLE multiblock solver for turbulent flow in complex domains. Technical report, Dept. of Thermo and Fluid Dynamics, Chalmers University of Technology, Gothenburg, 1998.

[19] W. Michael, D. Rubin, and E. Krempl. *Introduction to Continuum Mechanics*. Butterworth Heinemann, 1996. ISBN 0-7506-2894-4.

[20] A. E. Perry and M. S. Chong. A description of eddying motions and flow patterns using critical-point concepts. *Ann. Rev. Fluid Mech.*, 19:125–155, 1987.

[21] Rutherford Aris. *Vectors, Tensors, and Bacis Equations of Fluid Mechanics*. Dover Publications, Inc., 1 edition, 1962. ISBN 0-486-66110-5.

[22] J. Jeong and F. Hussain. On the identification of a vortex. *Journal of Fluid Mechanics*, 285:69–94, February 1995.

[23] D. Sujudi and R. Haimes. Identification of swirling flow in 3-D vector fields. AIAA Paper AIAA 95-1715, 1995.

[24] D. Wu. Predictive prospects of unsteady detached-eddy simulations in industrial external aerodynamic flow simulations. Diploma thesis. matriculation number: 219949, Lehrstuhl fur Strmungslehre und Aerodynamishes Institute, Aachen, Germany, 2004.